# Amorphous Carbon Gold Nanocomposite Thin Films: Structural and Spectro-ellipsometric Analysis

Z. Montiel-González [a,*], S.E. Rodil [a], S. Muhl [a], A. Mendoza-Galván [b], L. Rodríguez-Fernández [c]

[a] Instituto de Investigaciones en Materiales, Universidad Nacional Autónoma de México, Circuito exterior s/n, Ciudad Universitaria, Coyoacán 04510, México D.F, México
[b] Centro de Investigación y de Estudios Avanzados del Instituto Politécnico Nacional, Unidad Querétaro, 76010 Querétaro, Querétaro, México
[c] Instituto de Física, Universidad Nacional Autónoma de México, Circuito de la Investigación Científica, Ciudad Universitaria, 04510, México D.F, México

## ARTICLE INFO

## ABSTRACT

Spectroscopic Ellipsometry was used to determine the optical and structural properties of amorphous carbon: gold nanocomposite thin films deposited by dc magnetron co-sputtering at different deposition power. The incorporation of gold as small particles distributed in the amorphous carbon matrix was confirmed by X-ray Diffraction, Rutherford Backscattering measurements and High Resolution Transmission Electron Microscopy. Based on these results, an optical model for the films was developed using the Maxwell–Garnett effective medium with the Drude–Lorentz model representing the optical response of gold and the Tauc–Lorentz model for the amorphous carbon. The gold volume fraction and particle size obtained from the fitting processes were comparable to those from the physical characterization. The analysis of the ellipsometric spectra for all the samples showed strong changes in the optical properties of the carbon films as a consequence of the gold incorporation. These changes were correlated to the structural modification observed by Raman Spectroscopy, which indicated a clustering of the $sp^2$ phase with a subsequent decrease in the optical gap. Finally, measurements of Reflection and Transmission Spectroscopy were carried out and Transmission Electron Microscopy images were obtained in order to support the ellipsometric model results.

© 2011 Elsevier B.V. All rights reserved.

## 1. Introduction

Nanocomposite thin films consisting of nanoparticles (NPs) or nanocrystals embedded in a matrix have recently been the subject of many studies motivated by the extraordinary properties obtained in comparison to single-phase thin films.

For optical applications, metal NPs embedded in a dielectric matrix have demonstrated big third order non-linearity, which have potential for a plethora of applications. The existence of surface plasmon resonance of the metallic (Ag, Au, and Cu) nanocrystals in the visible region of the spectra, when dielectric matrices, such as $SiO_2$ or $TiO_2$ are used, have been widely investigated by optical techniques [1–3]. Dalacu and Martinu [4] have extensively used Spectroscopic Ellipsometry (SE) to investigate the nanostructural features of metal-dielectric nanocomposite thin films showing the potential of that technique as a non-destructive optical method giving information, not just of the optical properties, but about the morphology and the structure of the analyzed materials.

Amorphous carbon (a-C) was chosen as the matrix because the ellipsometric models of such films are well known, as well as, the film properties. Moreover, amorphous carbon:gold nanocomposite (a-C:Au) could be a candidate for catalytic applications, given the well-known CO oxidation properties of gold NPs [5]. The gold NPs are usually embedded in a $TiO_2$ matrix, although there is interest in studying the fundamentals of the catalytic properties of gold NPs and therefore different matrices are being used [6,7]. In this work, we have used SE to investigate metal-semiconductor nanocomposite thin films composed of gold NPs embedded in a low-bandgap a-C matrix. For the a-C:Au films there was no clear evidence of the surface plasmon resonance in the visible range. However, using information obtained from X-ray Diffraction (XRD) and Rutherford Backscattering (RBS) about the segregation of the gold phase as nanocrystals in the carbon matrix, the nanostructure features could be obtained by modeling the ellipsometric spectra using a Maxwell–Garnett effective medium.

## 2. Experimental details

### 2.1. Thin film deposition

The thin films were deposited on Si (111) and corning glass substrates, previously cleaned by ultrasonic bath, by dc magnetron co-sputtering in a homemade sputtering chamber. The substrate holder was fixed at $2.8 \times 10^{-2}$ m from the target and was rotated at constant speed (~80 rpm) during the deposition process, this setup is based on previous works concerning the deposition of nanocomposites by co-

* Corresponding author. Tel.: +52 55 56224734; fax: +52 55 56161251.
  E-mail address: zeuzmontiel@hotmail.com (Z. Montiel-González).

sputtering [8,9]. In order to determine the effect of the presence of Au in the a-C matrix, two sets of films were deposited under the same conditions for each experiment, one of them was a-C films and the other a-C:Au films. For samples of a-C, a graphite target was used. And for the a-C:Au films, a 99.99% pure Au piece was added such that about 2.6% of the area of graphite target erosion race track was covered. The deposition was done using pure argon (99.997%) plasma and the power was varied between 40 and 130 W in steps of 30 W, the deposition time was adjusted to give approximately the same thickness for all the samples. All the other deposition conditions were kept constants and are summarized in Table 1.

### 2.2. Characterization

#### 2.2.1. Composition and microstructure

Stylus profilometry, Veeco Dektak 150, was used for the thickness measurements in order to determine the deposition rate and for comparison with the values obtained from SE. The thickness was measured in a step produced by masking one small zone of the substrate around the edge. The surface morphology images were obtained from an Atomic Force Microscope (AFM) Jeol JSPM-4210 with the tapping mode. The RBS experiments were performed using 0.7 MeV $^4$He$^{+2}$ ions impinging on the sample at normal incidence and backscattered particles were registered at 135°. The RBS spectra were analyzed using the RUMP code [10] and the atomic composition of the films was determined. The XRD measurements were carried out using Cu K$\alpha_{1,2}$ radiation from a Siemens D500 diffractometer in the grazing angle configuration.

#### 2.2.2. Optical

The films deposited on Si (111) wafers were measured using a Phase Modulated Ellipsometer Uvisel Jobin Yvon DH10 in the photon energy range of 1.5 to 5.0 eV, with steps of 0.05 eV, at 70° incidence angle. The ellipsometric spectra were measure at two different modulator and analyzer configurations (high accuracy mode). The ellipsometric data analysis was performed with the DeltaPsi™2 software supplied by Horiba Jobin Yvon.

#### 2.2.3. Modeling process

Ellipsometry measures the change in the polarization state of the light beam after being reflected from a surface. The parameters measured with this optical technique are the ellipsometric angles psi ($\Psi$) and delta ($\Delta$). Such angles are related to the change of the polarization state through the Fresnel complex reflection coefficients by means of the fundamental equation of ellipsometry:

$$\rho = \frac{r_p}{r_s} = tan\Psi \, exp(i\Delta), \tag{1}$$

where $r_p$ and $r_s$ are the complex reflection coefficients parallel and perpendicular to the plane of incidence and $\rho$ is the change in the polarization state.
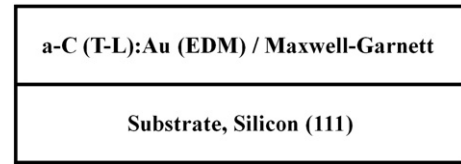


Fig. 1. The physical model used to represent the optical response of the nanocomposite films.

Ellipsometry is an indirect technique and the information is obtained from optical models. The basic parameters usually defined as unknowns in the optical models are the complex refractive index $N$ (dielectric function, $\varepsilon$) and the film thickness. The analysis of ellipsometric data to determine the values of the optical and structural parameters was carried out using the Marquardt–Levenberg fitting algorithm [11].

For materials comprised by two or more constituents or phases, the use of effective medium theories, such as those proposed by Maxwell–Garnett (M–G) and Bruggeman, have proven to be useful to obtain good approximations about properties of the mixture, such as volume fractions. However, those theories must be carefully applied because of the restrictions in their derivation and their misuse can result in meaningless physical parameters. The available theories determine the effective dielectric function as a function of the volume fractions and the dielectric function of the constituents in the mixture. One of the theories more often used for nanocomposite systems is that proposed by M–G which for two components is expressed as [12]:

$$\frac{\varepsilon_{M-G} - \varepsilon_b}{\varepsilon_{M-G} + 2\varepsilon_b} = f_a \frac{\varepsilon_a - \varepsilon_b}{\varepsilon_a + 2\varepsilon_b}, \tag{2}$$

where $\varepsilon_{M-G}$ is the effective dielectric function of the mixture, $\varepsilon_a$ is the dielectric function of the guest material (inclusions), $\varepsilon_b$ is the dielectric function of the matrix or host and $f_a$ is the volume fraction of the $a$ component. This theory describes a geometry consisting of randomly dispersed inclusions in the bulk of the matrix. The inclusions are assumed to have spherical shape and uniform size much less than the typical separation between them and that such separation is much less than the wavelength of the probe light. The M–G theory has been extensively used to describe the localized surface plasmon resonance of noble metal NPs embedded in insulator matrices [12]. Therefore, the ellipsometric analysis of the a-C:Au nanocomposite films, which showed (by means of XRD, RBS and Transmission Electron Microscopy, TEM) gold nanophase inclusions well dispersed in the matrix, was carried out using the model shown in Fig. 1. This model considers the presence of homogeneously distributed Au NPs in the bulk of the a-C matrix. Additionally, the model is a two layered system where the first layer is the Si substrate and the second layer is the M–G effective medium constituted by a-C and Au.

**Table 1**
General deposition conditions for both groups of films, a-C and a-C:Au.

| Sample | a-C40W, a-C:Au40W | a-C70W, a-C:Au70W | a-C100W, a-C:Au100W | a-C130W, a-C:Au130W |
|---|---|---|---|---|
| Power (Watts) | 40 | 70 | 100 | 130 |
| Deposition time (s) | 2400 | 1110 | 780 | 510 |
| Base pressure (Pa) | $6.7 \times 10^{-4}$ | | | |
| Deposition pressure (Pa) | 2.7 | | | |
| Ar flow (sccm) | 10 | | | |
| Target-substrate distance (m) | $2.8 \times 10^{-2}$ | | | |
| Substrate temperature (°C) | No heating. max. 100 | | | |

In the M–G approximation, the dielectric function of the a-C component was parameterized using the Tauc–Lorentz (T–L) model, the most extensively used for amorphous semiconductors [13]:

$$\varepsilon_2(E)^2 = \begin{cases} \left[ \dfrac{AE_0C\left(E-E_g\right)^2}{\left(E^2-E_0^2\right)^2 + C^2E^2} \cdot \dfrac{1}{E} \right], E > E_g \\ 0, E \le E_g \end{cases} \tag{3}$$

this expression contains four fitting parameters: the bandgap, $E_g$, of the material, the peak of the joint density of states $E_0$, the amplitude of the optical transition $A$ and the broadening of the absorption peak $C$. The real part is calculated by performing the Kramers–Kronig integration.

The dielectric function of the metals can be represented by the contribution of the free electrons (intraband transitions), bound electrons (interband transitions) and the collective oscillations of the free electrons known as plasma behavior. In the case of noble metals some features in the electronic structure, for example, the separation between the conduction band ($s$ bands) and the valence band ($d$ bands) produces an effect on the behavior of the conduction electrons, changing their optical response. For noble metals the separation of the contribution of free electrons from the effect produced by $d$ electrons is not straightforward and the application of a suitable dispersion relation is a complicated task [14]. In this work, the gold dielectric function, in the photon energy range of interest (1.5–5.0 eV) was simulated using an extended Drude model (EDM) [15], containing the Drude free-electron absorption with five Lorentz oscillators [16], as shown in Eq. (4):

$$\varepsilon(\omega) = \varepsilon_\infty + \frac{\omega_p^2}{-\omega^2 + i\Gamma_D\omega} + \sum_{j=1}^{5} \frac{f_j\omega_{0j}^2}{\omega_{0j}^2-\omega^2 + i\gamma_j\omega}, \tag{4}$$

where, $\varepsilon_\infty$ is the dielectric function at high frequencies, $\omega_p$ is the plasma frequency, $\Gamma_D$ is the damping coefficient related with the mean free path (mfp) of the electrons and $\omega_{0j}$, $f_j$ and $\gamma_j$ are the position, amplitude and damping of the jth Lorentz oscillator, respectively. The precise values of the parameters in Eq. (4) were obtained by fitting the reference data for gold supplied in the DeltaPsi™2 software.

In the case of NPs it is necessary to consider the size of the particle in comparison to the mfp of the electrons (bulk crystalline gold ~40 nm) [17]. For a particle size larger than the mfp, the dielectric function can be taken from the optical referenced data for bulk Au. On the other hand, for sizes smaller than the mfp, it is necessary to make a correction to the damping coefficient $\Gamma_D$ in order to take into account the border size effects. Because $\Gamma_D \sim \tau^{-1}$, being $\tau$ the relaxation time of electrons, border effects are related to the size of the NPs through the following relationship [18]:

$$\tau_p^{-1} = \tau_B^{-1} + {}^{\nu_F}\!/_{a}, \tag{5}$$

where $\tau_p$ is the relaxation time of the particles, $\tau_B$ is the bulk relaxation time in Au ($2.57 \times 10^{-14}$ s), $\nu_F$ is the Au Fermi velocity ($1.39 \times 10^6$ m/s) and $a$ is the radius of the particle.

Once that the T–L parameters of the a-C matrix were determined, the analysis of the SE data for the nanocomposite a-C:Au thin films was carried out as follows: first, the thickness, volume fraction and damping coefficient ($\Gamma_D$) in the Drude term of the Au-EDM were optimized in the fitting process. The next step was to fix the latter values obtained and then the parameters of the T–L a-C matrix were allowed to vary. This step was required since the Raman analysis indicated that the a-C matrix bonding characteristics were slightly modified by the co-deposition of gold. In the final step, only the damping coefficient and the plasma frequency ($\omega_p$) of the Au-EDM were fitted. Thus, from the fitted value of $\Gamma_D$ ($=\hbar/\tau_p$) and Eq. (5) the

average size of the gold inclusions could be estimated. This step-fitting procedure was chosen due to the complexity of the system; if all the a-C matrix and Au parameters were optimized simultaneously, the best fitting resulted in a zero gold content and strong, somewhat unrealistic, changes in the optical properties of the carbon matrix. Then, the n&k values did not represent a typical amorphous carbon matrix and the results were not consistent with the fact that XRD, RBS and TEM showed the presence of gold. Nevertheless, by doing fittings from different initial parameters which always lead to similar solutions, we corroborated that the solution presented here is close to the global minimum.

### 2.2.4. Complementary characterization

The Raman spectra of the samples deposited on Si were obtained using a Horiba Jobin Yvon LabRam HR high resolution Raman spectrometer with a green line laser (532.07 nm). Finally, a Film Tek 3000™ equipment in the spectral range of 240–840 nm was used to obtain the Reflection (both Si and glass substrates) and transmission (corning glass substrate) spectra at normal incidence. High resolution TEM images of the cross section of selected samples were obtained in a JEM-2200FS microscope in the scanning mode (STEM) using the bright field and Z contrast detectors.

## 3. Results and discussion

### 3.1. Film growth (profilometry and AFM)

The deposition rate of a-C and a-C:Au films as a function of sputtering power is shown in Fig. 2. As can be noticed the film growth rate increased slightly with the inclusion of the small piece of gold on the target and follows a nearly linear dependence on the sputtering power investigated. A similar phenomenon was reported in a previous paper from our group when silver was added to a-C films [9]. A likely explanation is that the Au increases the secondary electrons production increasing the plasma density, which enhances ion flux on the target increasing the erosion rate. This explanation requires further detailed studies, nevertheless is in agreement with the ideas presented in the work of Depla et al. [19].

Fig. 3 shows AFM images of a-C and a-C:Au films deposited at the sputtering power of 130 W. It can be noticed that the features of the a-C:Au films were finer than those of the a-C films, and that both samples were of uniform roughness (2.59 nm and 7.23 nm RMS values for films with and without Au, respectively). Similar differences in the morphology were observed for the films, with and without gold, produced at the other plasma powers.

Considering that these values were relatively small and to keep the ellipsometric model as simple as possible, no roughness layer was included.
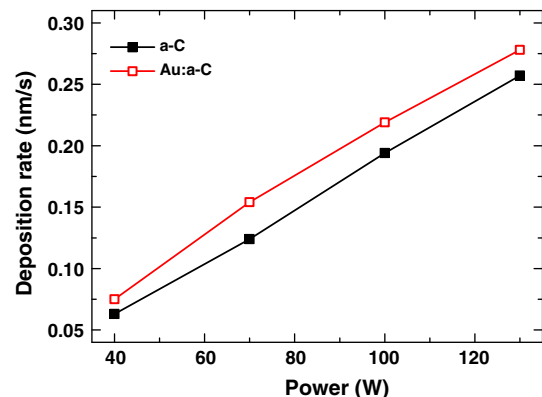


Fig. 2. Deposition rates calculated from profilometry measurements of the a-C and a-C: Au films deposited at the same conditions.
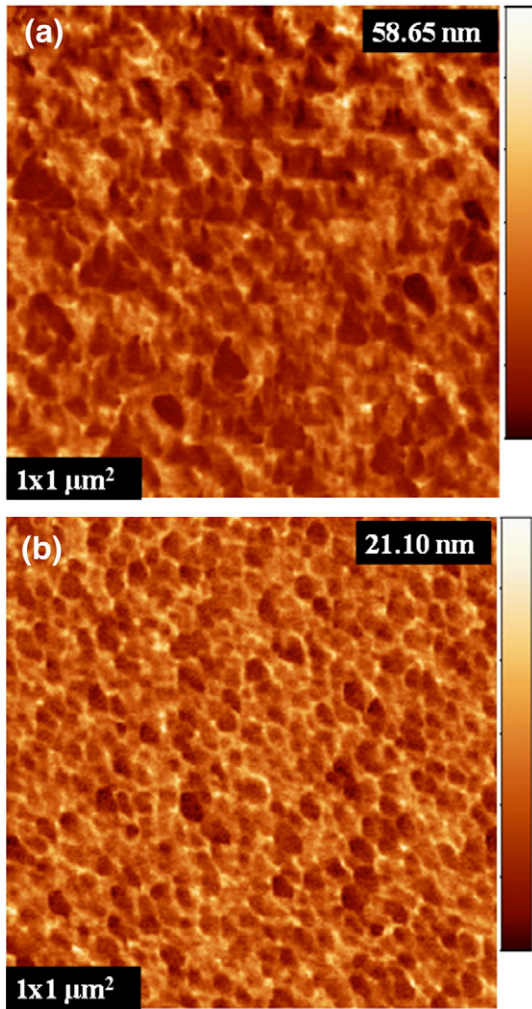
**Fig. 3.** AFM morphology images of (a) a-C130W and (b) a-C:Au130W films deposited using the same conditions.

## 3.2. Composition (RBS)

Fig. 4 shows the experimental RBS data and the RUMP simulation spectrum for the a-C:Au 70 W sample. The simulation of the spectrum not only indicates the film composition, but also provided information about the composition profile in the film [20]. On one hand, the form of the amplitude versus energy of the C and Au signals was very similar, which indicated that the distribution of Au in the a-C matrix



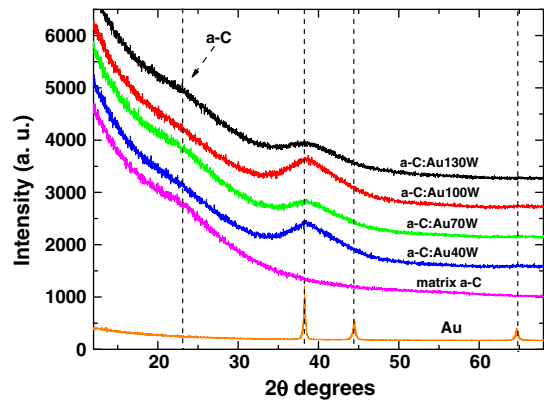**Fig. 4.** RBS spectra of the a-C:Au70W nanocomposite film and the RUMP simulation.



**Fig. 5.** XRD patterns for all the nanocomposite films.

was uniform throughout the thickness of the film. The gold content ranged from 6.5 to 8.5 at.% without any clear trend with the deposition power, as reported later in Table 4. The atomic densities were determined by dividing the areal density by the thickness obtained from SE and were about $8 \times 10^{22}$ at/cm$^3$, again without any clear trend.

### 3.3. Microstructure (XRD)

Fig. 5 shows the XRD patterns for the a-C:Au films as well as data from a pure gold standard and the a-C matrix. Two small signals could be seen in the patterns of the nanocomposites, one corresponds to the a-C matrix (about 23° in 2θ) and the other around ~38° (2θ) corresponds to the most intense peak for fcc gold (JCPDS 4–784). An estimation of the grain size was done using the total full width half maximum of the gold peak and the Scherrer formula, without correcting for strain or instrumental broadening effects. Then, the approximate crystal grains obtained were lower than 2 nm, as shown in Table 2.

### 3.4. Ellipsometric fittings

#### 3.4.1. Amorphous carbon matrix

Fig. 6 shows the experimental and best fit SE data. The fitting figure of merit $\chi^2$ and the values of the T–L parameters; oscillator energy, $E_0$ associated to the $\pi-\pi^*$ transitions [21] and optical gap, $E_g$ are shown in Table 3 as well as the thicknesses obtained by SE and profilometry for comparison.

#### 3.4.2. a-C:Au nanocomposite thin films

The experimental and best fit ellipsometric spectra for the a-C:Au samples are shown in Fig. 7. By comparing Figs. 6 and 7 it can be noticed that the presence of Au in the a-C matrix produces a significant change in the ellipsometric spectra. This variation could not be explained by the thickness difference among the a-C and a-C: Au samples, as was confirmed by simulating the spectra of the a-C matrix for different thicknesses using the T–L parameters reported in Table 3. Therefore, we concluded that the changes could be taken as evidence of the incorporation of gold, however, we did not observed

**Table 2**
The grain size obtained from the Scherrer analysis of the 38° broad peak, where the FWHM was obtained from fitting the peak using a Gaussian formula and r$^2$ indicates the correlation from this fitting.

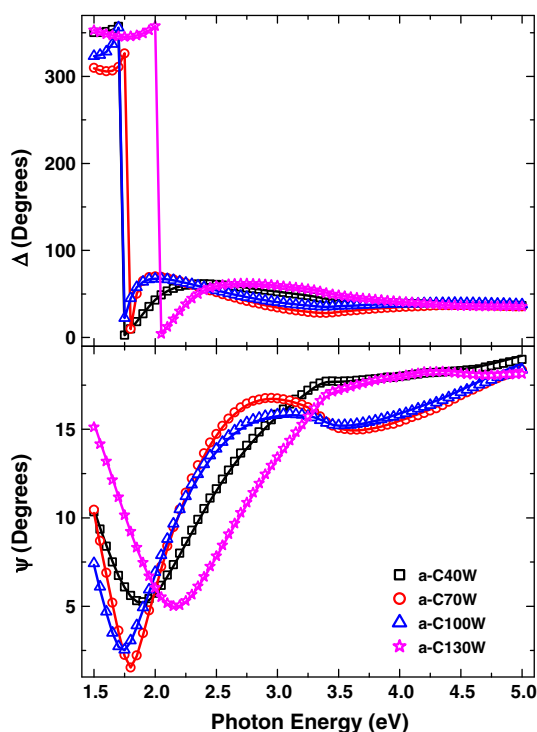| Sample | r$^2$ | FWHM (rad) | Grain size (nm) |
|---|---|---|---|
| a-C40W | 0.94 | 5.99 | 1.41 |
| a-C70W | 0.96 | 5.50 | 1.52 |
| a-C100W | 0.97 | 6.27 | 1.33 |
| a-C130W | 0.95 | 6.43 | 1.30 |

**Fig. 6.** Experimental (symbols) and best fit (lines) ellipsometric spectra ($\Psi$ and $\Delta$) of a-C films.

any sharp absorption peak associated with the surface plasmon resonance of gold NPs, as has been observed when gold NPs are embedded in insulating and transparent matrices. The surface plasmon resonance (SPR) of 10 nm gold nanoparticles in vacuum was calculated to be at 2.4 eV (520 nm) [22]. When these NPs are embedded in a matrix, the energy is expected to decrease when either the concentration or the size increased or when the refractive index of the matrix increased. It has also been determined that as the size decreased below 10 nm, the intensity tends to decrease and the width broadens due to quantum size effects [22]. Therefore, we expected to observe a particular signal (corresponding to the gold SPR) around 2.0–2.4 nm, but this was not so evident.

From the fittings (lines) in Fig. 7, it is clear that a good agreement between the experimental and the calculated spectra was obtained. The latter is also reflected by the small figure of merit $\chi^2$ as shown in Table 4, where the summary of the fitted values for the most relevant parameters are shown, no significant differences were obtained for the other parameters.

### 3.5. Structural information from SE

As shown in Table 4, the thickness obtained from the ellipsometric analysis and profilometry showed a relative good agreement,

**Table 3**
The Tauc–Lorentz parameters for the a-C matrix and thicknesses obtained by profilometry. The errors associated with the ellipsometric measurements correspond to 90% of confidence. For the profilometry five measurements on the same sample were performed.

| Sample | $\chi^2$ | $E_g$ (eV) | $E_0$ (eV) | Thickness (nm) | |
|---|---|---|---|---|---|
| | | Tauc–Lorentz | | SE | Prof. |
| a-C40W | 0.02 | $0.14 \pm 0.01$ | $6.00 \pm 0.04$ | $151 \pm 0.20$ | $152 \pm 2.90$ |
| a-C70W | 0.02 | $0.39 \pm 0.01$ | $5.87 \pm 0.02$ | $179 \pm 0.19$ | $171 \pm 3.90$ |
| a-C100W | 0.02 | $0.21 \pm 0.01$ | $5.90 \pm 0.03$ | $172 \pm 0.22$ | $171 \pm 2.60$ |
| a-C130W | 0.02 | $0.24 \pm 0.01$ | $6.16 \pm 0.05$ | $135 \pm 0.17$ | $131 \pm 4.30$ |

considering that the region where ellipsometric and profilometry measurements are done, is not exactly the same. The new T–L parameters for the a-C matrix of the composite films showed decreasing values of both the bandgap and the position of $E_0$, but still lying in the range reported for a-C films [21,23].

The "average" Au NPs size calculated from the damping coefficient as described in Eq. (5) showed an increase from 4 nm to 8 nm as the power increased, but in any case was larger than those obtained by XRD. The differences in particle size between XRD and other techniques have been observed in previous studies [24] and different solutions to analyze properly the XRD data have been proposed. Hall et al. [25] studying gold nanoparticles concluded that a Fourier analysis method instead of the Scherrer equation could lead to better correlation between XRD and TEM size analysis. However, in our case there are no enough diffraction peaks from the gold to make a Fourier analysis. It is also important to consider that the M–G model assumes a uniform particle size, while most probably the films have a size distribution of NPs, as observed in the TEM images.

Finally, Table 4 also includes the atomic Au content estimated from the fitted volume fraction obtained in the effective medium model and the density of both Au (19.3 g/cm³) and a-C (1.72 g/cm³) as taken from Ferrari et al. [26]. It is important to note that the atomic contents are not very far from those obtained from the RBS analysis (also shown in Table 4) and indeed the small differences could be explained as a consequence of the real density of a-C matrix, which has not been measured. If the density is allowed to change from 1.2 g/cm³ to 2 g/cm³ as the power increased, the atomic concentration will have agreed well to the RBS data. Carbon film densities as low as 1.2 g/cm³ have been reported for hydrogenated carbon films [26], which is not our case. However, 40 W is a very low power density, which we expected to produce porous and floppy carbon films.

### 3.6. Optical properties from SE

The optical constants; the refractive index ($n$) and the extinction coefficient ($k$), for the a-C and the a-C:Au films are shown in Fig. 8. For the nanocomposites, the values plotted are the effective optical constants. The most significant difference is the increment in the extinction coefficient for the a-C:Au nanocomposites compared to the a-C films, which is in good agreement with the lower optical gap of the a-C:Au films, shown in Tables 3 and 4. The refractive indexes of the a-C films are in the range reported for sputtered a-C films [23] and for the nanocomposites, at high energies, the values are similar. However, for energies below 3 eV, there is an increment in the $n_{eff}$ for the a-C:Au films, which indicates a higher film density.

### 3.7. Complementary characterization

#### 3.7.1. Raman spectroscopy

Fig. 9a shows the Raman spectra from the a-C100W matrix and the a-C:Au100W samples, similar spectra were observed for the other plasma powers. The Raman spectra have the typical characteristic of amorphous carbon films: a broad peak centered at approximately 1550 cm$^{-1}$ that is usually fitted using two peaks at approximately 1560 cm$^{-1}$ (G band) and 1360 cm$^{-1}$ (D band). The G band represents the C–C $sp^2$ bonds and the presence of the D band indicates the formation of aromatic rings/clusters in the $sp^2$ phase. The I(D)/I(G) intensity ratio is considered to reflect the size of the aromatic clusters in disordered carbons [27]. The spectra were analyzed using Lorentzian (G) and Breit–Wigner–Fano (D) functions to fit the data and the obtained G peak position (G pos), G width and I(D)/I(G) are shown in Fig. 9b, c and d, respectively. There was no large variation with the plasma power for the a-C and a-C:Au groups. However, there was a clear tendency of clustering of the $sp^2$ phase when gold was incorporated into the a-C matrix, since both the G position and I(D)/I
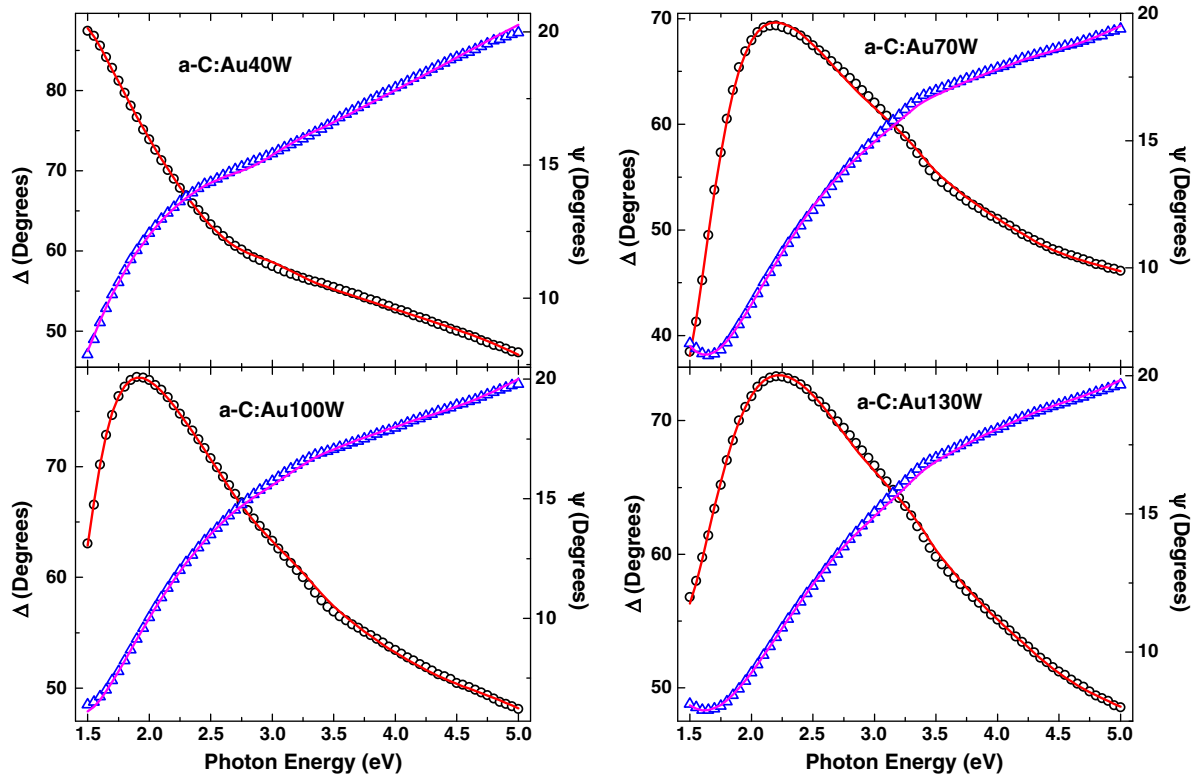
**Fig. 7.** Experimental and best fit spectra of $\Psi$ and $\Delta$ for the a-C:Au films. The symbols are the measured data ($\Delta$-circles and $\Psi$-triangles) and the line corresponds to the fitting.

(G) ratio increased while the G width decreased. This is a common result for metal containing a-C films [27].

It is also important to note that clustering of the $sp^2$ phase is usually associated with a decrease in the optical gap [21,27]; larger clustering or larger I(D)/I(G) ratios correspond to films having smaller bandgaps. This trend was also observed in the present work when the $E_g$ reported in Tables 3 and 4 are compared.

### 3.7.2. Reflection and transmission spectra

In general, the reflectance and transmittance of a system are function of the complex refractive index of the media involved, the thicknesses between the different layers and the wavelength and incidence angle of the probe light [28]. As was discussed above, those parameters were obtained from the ellipsometric fitting process and, in consequence, the reflectance and transmittance spectra could be estimated. As a proof of consistency, model-calculated transmittance and reflectance spectra can be compared with the measured optical spectra.

Fig. 10a shows the transmittance calculated for a glass substrate for the a-C:Au70W sample and the measured transmittance for an a-C:Au70W sample deposited on glass.

Fig. 10b shows the reflectance spectra for both types of substrates; glass and silicon. There was a very good agreement for the

transmittance spectra, while the agreement for the reflectance spectra was less precise, with differences of about 2.0% in the reflectance value. Nevertheless, the spectra features are well reproduced and overall, we considered that the similitude between measured and calculated spectra was a good indication of the reliability of the ellipsometric model used.

### 3.7.3. Transmission Electron Microscopy

Fig. 11 shows the scanning electron transmission micrographs obtained from the nanocomposite sample a-C:Au70W. Fig. 11a shows the bright-field image where the gold inclusions are observed as dark spots. Meanwhile Fig. 11b is a Z contrast image of the same region and gold appears as bright spots. Line scan EDS confirmed that the bright spots were mainly composed of gold, as observed in Fig. 11c. Finally, the crystalline gold NPs were observed in Fig. 12 and many of them were found to be distributed throughout the film thickness. The particle size showed variations between 5 and 12 nm, however no statistical analysis was made. These sizes are larger than those obtained from XRD, but closer to the ellipsometric results. Slightly less particles were observed for the a-C:Au130W, which was also examined, but in general similar gold distribution and sizes were observed.

**Table 4**
Summary of results of the fitting processes for the nanocomposite films.

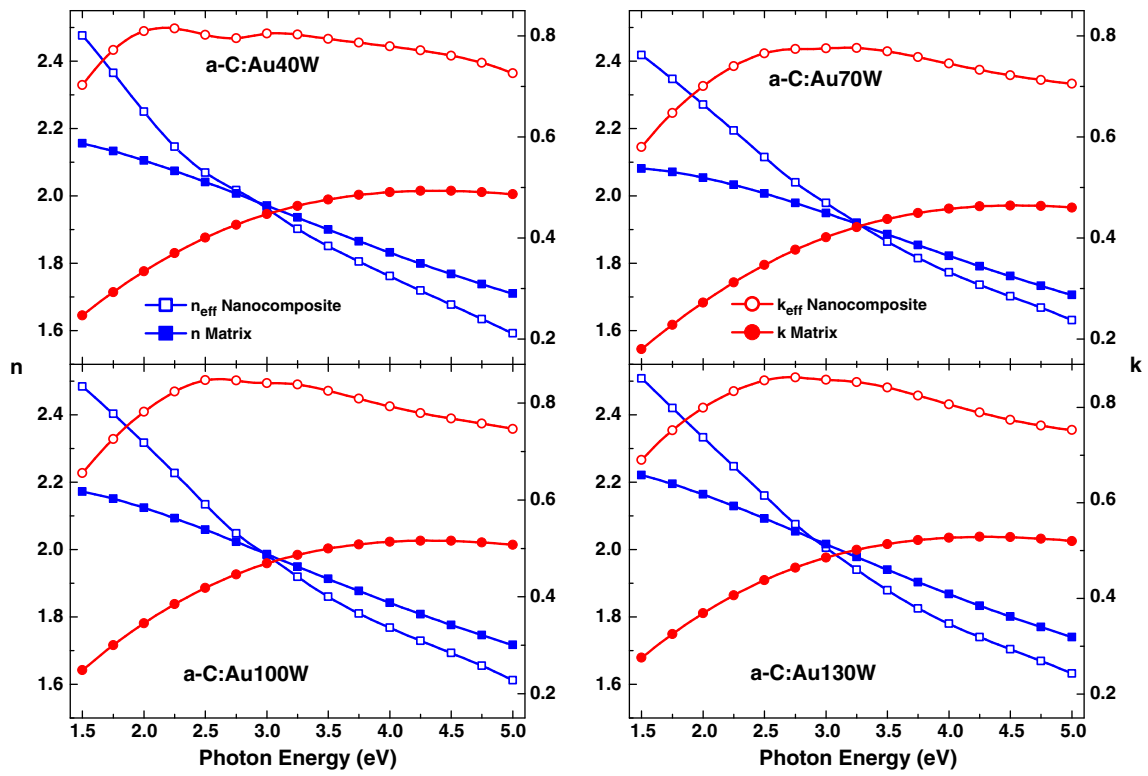| Sample a-C:Au | $\chi^2$ | Tauc–Lorentz matrix | | Thickness | | Particle size Au-EDM | | Gold content | | |
|---|---|---|---|---|---|---|---|---|---|---|
| Power (Watts) | | $E_g$ (eV) | $E_0$ (eV) | SE (nm) | Prof. (nm) | $\Gamma_D$ (eV) | Size (nm) | $f_v$ SE (% v) | $f_{at}$ SE (% at) | $f_{at}$ RBS (% at) |
| 40 | 0.03 | $0.09 \pm 0.02$ | $5.83 \pm 0.14$ | $183 \pm 0.54$ | $180 \pm 6.70$ | $1.56 \pm 0.02$ | $4.11 \pm 0.06$ | $7.85 \pm 0.03$ | $5.6 \pm 0.03$ | $7.92 \pm 0.8$ |
| 70 | 0.05 | $0.17 \pm 0.02$ | $4.81 \pm 0.11$ | $139 \pm 0.12$ | $138 \pm 4.40$ | $1.54 \pm 0.02$ | $4.17 \pm 0.06$ | $12.91 \pm 0.02$ | $9.3 \pm 0.02$ | $8.42 \pm 0.8$ |
| 100 | 0.03 | $0.13 \pm 0.01$ | $5.45 \pm 0.12$ | $146 \pm 0.12$ | $150 \pm 3.40$ | $1.22 \pm 0.01$ | $5.42 \pm 0.05$ | $11.55 \pm 0.01$ | $8.5 \pm 0.01$ | $6.98 \pm 0.7$ |
| 130 | 0.03 | $0.12 \pm 0.02$ | $4.79 \pm 0.12$ | $126 \pm 0.12$ | $142 \pm 1.00$ | $0.88 \pm 0.01$ | $7.99 \pm 0.11$ | $11.39 \pm 0.01$ | $7.8 \pm 0.01$ | $6.72 \pm 0.7$ |

**Fig. 8.** Optical constants (*n*&*k*) of a-C films and a-C:Au obtained from the fitting processes.
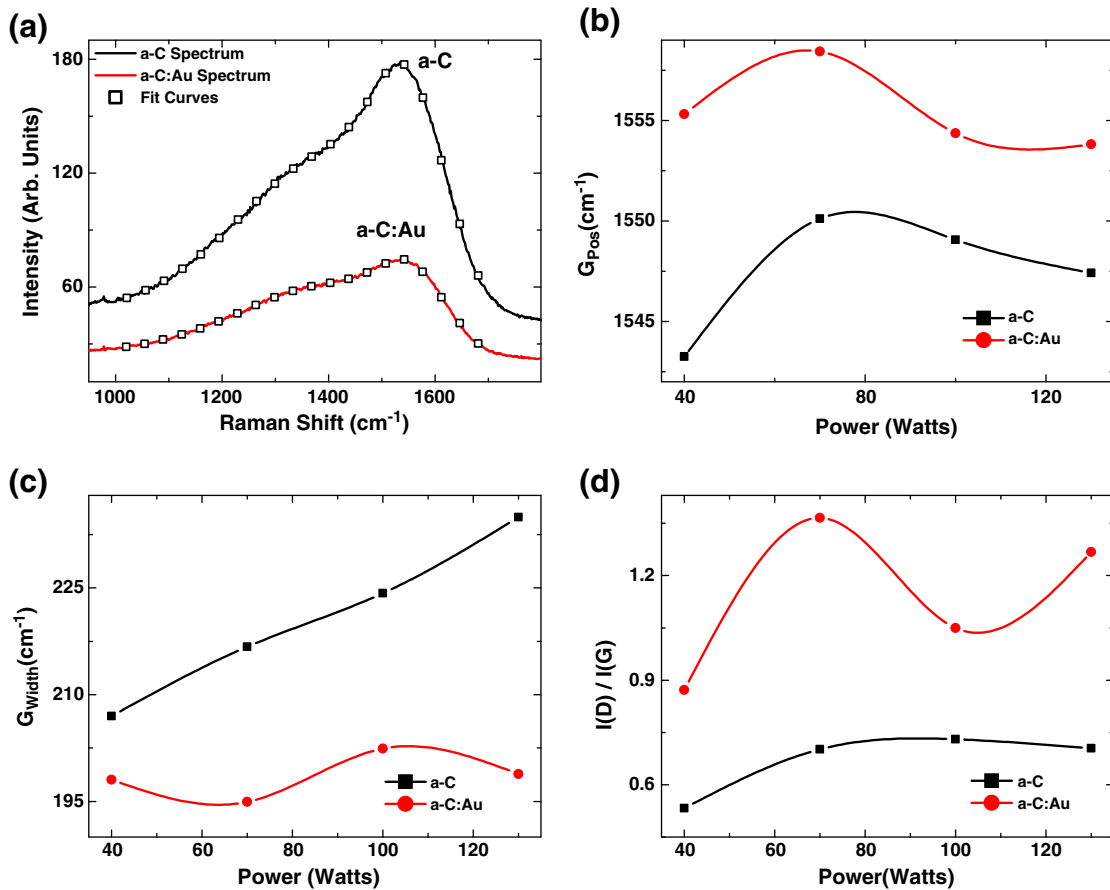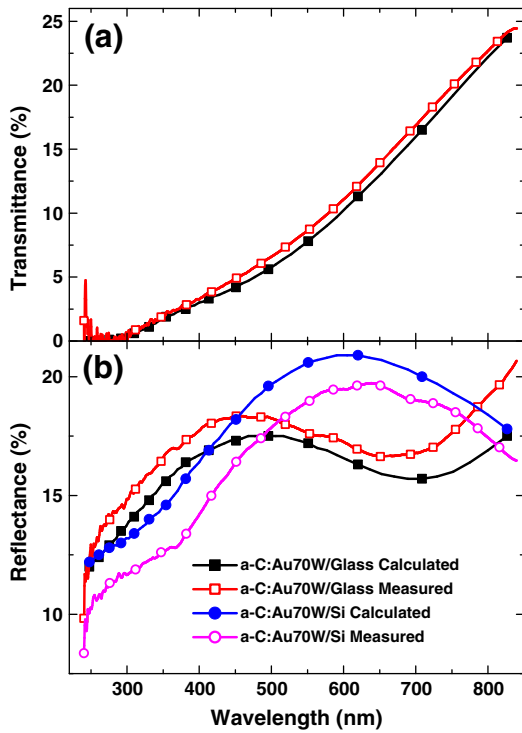


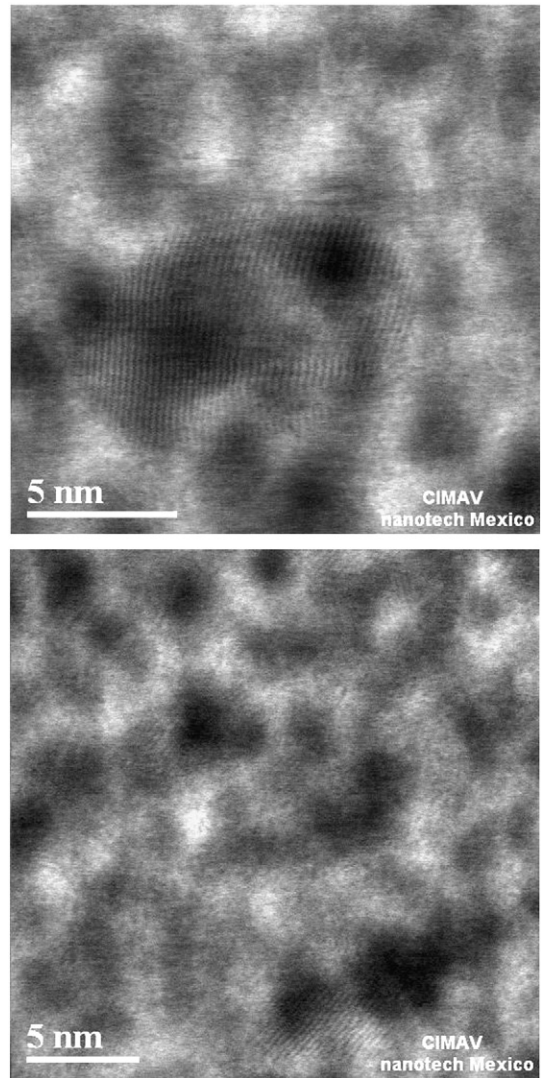**Fig. 9.** Raman spectra and analysis for a-C and a-C:Au films.

**Fig. 10.** (a) Transmittance spectra measured and calculated of glass substrate samples and (b) reflectance spectra measured and calculated for both glass and silicon substrates. The spectra correspond to the a-C:Au70W film.
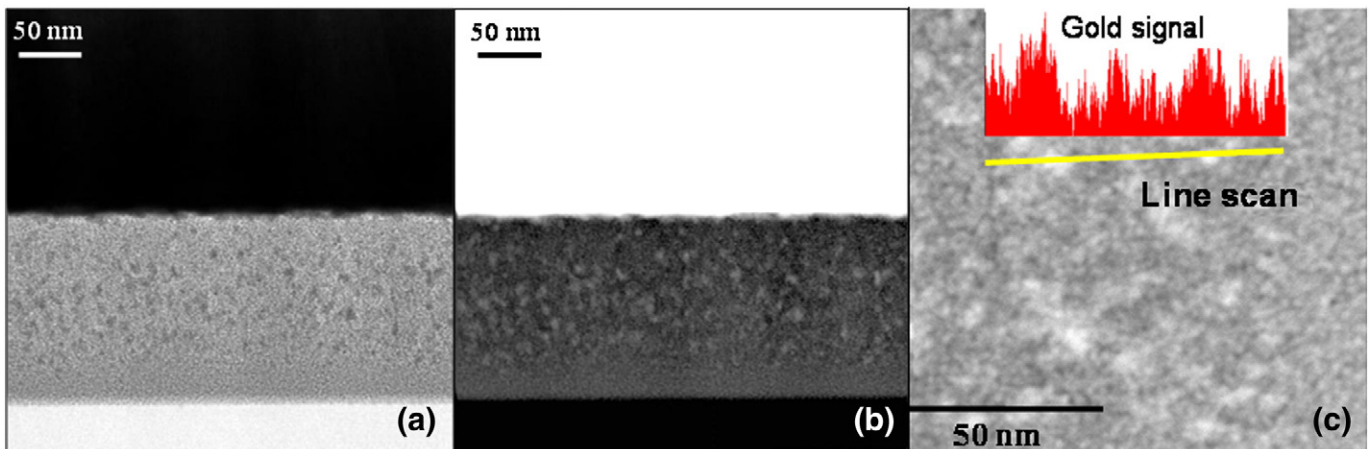
## 4. Conclusions

Nanocomposite thin films of gold nanoparticles embedded in a-C matrix were fabricated using magnetron co-sputtering from a graphite target having a small piece of pure gold (0.56 cm$^2$) attached to the race-track area. The chemical, structural, optical and bonding characteristics of these films were evaluated as a function of the plasma power. The films formed nanocomposites where carbon was the amorphous matrix and gold was included as small NPs.

The results obtained in this work indicated that, even though the gold surface plasmon was not observed in either the ellipsometric or transmittance spectra, using the evidence from the XRD, RBS and TEM of the presence of gold NPs it was possible to propose a parametric model using the Maxwell–Garnett approximation to obtain information about the size and concentration of the inclusions. The results in



**Fig. 12.** Crystalline gold grains in different regions of the a-C:Au70W film.

terms of particle size and atomic percentage obtained from the ellipsometric fitting are within the confidence limit and are similar to those obtained from the other techniques, such as, XRD and RBS. The main advantages of ellipsometry on other techniques are sampling on



**Fig. 11.** Transmission electron micrographs of the a-C:Au70W sample. (a) bright field, (b) Z-contrast and (c) EDS line scan.

millimeter areas, non-destructive and no sample preparation is required. Moreover, since ellipsometry is an indirect model-dependent technique, the reliability of the model needs to be tested by comparing model-calculated data with independent measured reflectance and transmittance spectra. The comparison between calculated and measured R and T spectra of the a-C:Au nanocomposite thin films was fairly good, giving reliability to the model results.

## Acknowledgments

## References

[1] L. Armelao, D. Barreca, G. Bottaro, A. Gasparotto, S. Gross, C. Maragno, E. Tondello, Coordin. Chem. Rev. 250 (2006) 1294.
[2] U. Pal, Sol. Energ. Mat. Sol. C. 81 (2004) 339.
[3] A. Mendoza-Galván, J.F. Pérez-Robles, F.J. Espinoza-Beltrán, R. Ramírez-Bon, Y.V. Vorobiev, J. González-Hernández, G. Martínez, J. Vac. Sci. Technol. A. 17 (1999) 1103.
[4] D. Dalacu, L. Martinu, J. Appl. Phys. 87 (2000) 228.
[5] M. Haruta, S. Tsubota, T. Kobayashi, H. Kageyama, M.J. Genet, B. Delmon, J. Catal. 144 (1993) 175.
[6] E. Thune, E. Carpene, K. Sauthoff, M. Seibt, P. Reinke, J. Appl. Phys. 98 (2005) 034304.
[7] M. Wanner, R. Werner, D. Gerthsen, Surf. Sci. 600 (2006) 632.
[8] V. Reillon, S. Berthier, S. Chenot, Physica B 394 (2007) 238.
[9] O. Garcia-Zarco, S. Rodil, M. Camacho-López, Thin Solid Films 518 (2009) 1493.
[10] L.R. Doolittle, Nucl. Instrum. Meth. B 15 (1986) 227.
[11] H.G. Tompkins, E.A. Irene, Handbook of Ellipsometry, William Andrew Publishing and Springer, United States of America, 2004.
[12] R.J. Gehr, R.W. Boyd, Chem. Mater. 8 (1996) 1807.
[13] G.E. Jellison, F.A. Modine, Appl. Phys. Lett. 69 (1996) 371.
[14] M. Suffczynski, Phys. Rev. 117 (1960) 663.
[15] C.F. Bohren, D.R. Huffman, Absorption and Scattering of Light by Small Particles, John Wiley & Sons, Unites States of America, 1983.
[16] A.D. Rakic, A.B. Djurisic, J.M. Elazar, M.L. Majewski, Appl. Optics. 37 (1998) 5271.
[17] B.R. Cooper, H. Ehreinreich, H.R. Philipp, Phys. Rev. 138 (1965) 494.
[18] U. Kreibig, M. Vollmer, Optical Properties of Metal Clusters, Springer, Germany, 1995.
[19] D. Depla, H. Tomaszewski, G. Buyle, R. Degryse, Surf. Coat. Tech. 201 (2006) 848.
[20] H.R. Verma, Atomic and Nuclear Analytical Methods, Springer, United States of America, 2007.
[21] S. Logothetidis, Diam. Relat. Mater. 12 (2003) 141.
[22] C.N.R. Rao, A. Müller, A.K. Cheetham, Nanomaterials Chemistry: Recent Developments and New Directions, John Wiley & Sons, United States of America, 2007.
[23] S. Logothetidis, M. Gioti, Mat. Sci. Eng. B 46 (1997) 119.
[24] H. Borchert, E.V. Shevchenko, A. Robert, I. Mekis, A. Kornowski, G. Grübel, H. Weller, Langmuir 21 (2005) 1931.
[25] B.D. Hall, D. Zanchet, D. Ugarte, J. Appl. Crystallogr. 33 (2000) 1335.
[26] A. Ferrari, A. Libassi, B. Tanner, V. Stolojan, J. Yuan, L. Brown, S. Rodil, B. Kleinsorge, J. Robertson, Phys. Rev. B. 62 (2000) 11089.
[27] A.C. Ferrari, J. Robertson, Philos. T. R. Soc. A 362 (2004) 2477.
[28] H.G. Tompkins, W.A. McGahan, Spectroscopic Ellipsometry and Reflectometry: A User's Guide, John Wiley & Sons, United States of America, 1999.